Energy & Environmental Science

Accepted Manuscript

This article can be cited before page numbers have been issued, to do this please use: W. Wang, C. Zhang, X. Ma, W. Wang, Q. Su, J. Long, D. Zhu, J. Li, A. Xu, R. Fang, Y. Dai, G. Gao and Q. An, *Energy Environ. Sci.*, 2026, DOI: 10.1039/D6EE01732K.

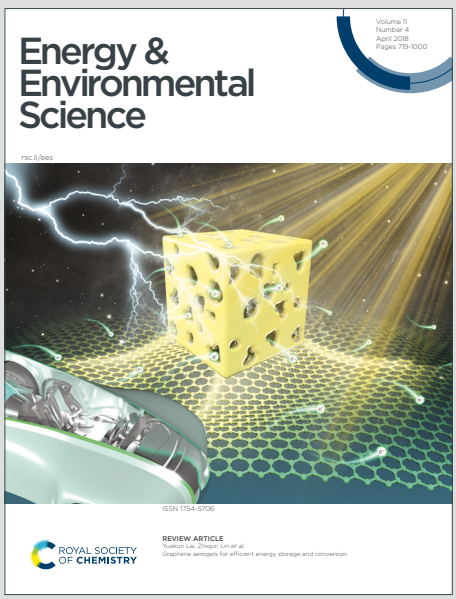

ROYAL SOCIETY OF CHEMISTRY

rsc.li/ees

View Article Online
DOI: 10.1039/D6EE01732K

Broader context

Rechargeable magnesium metal batteries could offer a safer and more abundant alternative to lithium-based systems, with the potential for high volumetric energy density. In practice, performance is often limited not by the bulk materials but by the thin layers (interphases) that form where the electrolyte meets the anode and the cathode. When these interphases are nonuniform or fracture during cycling, side reactions accelerate, and much of the theoretical charge-storage capacity becomes difficult to access. A key challenge is that cathodic and anodic interphases in full cells are coupled, so improving one can unintentionally worsen reactions at the other. This work shows that both interfaces must be controlled together to build continuous and uniform interphases on each electrode. An energy-level-guided electrolyte design steers electrolyte breakdown to electrode surfaces, enabling concurrent formation of protective interphases on both the anode and cathode. This stabilizes higher-capacity charge storage in $Mg||Mo_6S_8$ full cells, achieving state-of-the-art performance. More broadly, paired interphase control provides a general strategy for multivalent metal batteries, where long-term stability depends on coordinating the anode, cathode, and electrolyte as a single system.

Dual interphase design stabilized Mg-metal batteries

View Article Online
DOI: 10.1039/D6EE01732K

Wenwen Wang[1,#], Chengyi Zhang[2,#], Xinquan Ma[1,#], Weixiao Wang[1,#], Qin Su[1], Juncai Long[3], Dongyao Zhu[1], Jinghao Li[1], Ao Xu[1], Rui Fang[4], Yuhang Dai[5,*], Guanbin Gao[1,*], Qinyou An[1,*]

[1]State Key Laboratory of Advanced Technology for Materials Synthesis and Processing, Wuhan University of Technology, Wuhan 430070, PR China.

[2]School of Chemical Sciences, The University of Auckland, Auckland 1010, New Zealand.

[3]Department of Industrial and Systems Engineering, The Hong Kong Polytechnic University, Hung Hom, Hong Kong 999077, PR China.

[4]Department of Chemical and Environmental Engineering, University of Cincinnati, Cincinnati, OH 45220, USA.

[5]Institute for Integrated Cell-Material Sciences, Kyoto University, Yoshida, Sakyo-ku, Kyoto 606-8501, Japan.

[#]These authors contributed equally: Wenwen Wang, Chengyi Zhang, Xinquan Ma, and Weixiao Wang

[*]Corresponding emails: dai.yuhang.72z@st.kyoto-u.ac.jp (Y.D.); gbgao@whut.edu.cn (G.G.); anqinyou86@whut.edu.cn (Q.A.);

Abstract

Rechargeable magnesium metal batteries (RMBs) promise high volumetric energy density and resource sustainability, yet interphase instability remains a central barrier to practical full cells. Here, we show that single-electrode interphase stabilization often does not translate into durable full-cell operation, as instability can still emerge at the counter electrode during cycling. We therefore propose an energy-level-guided electrolyte design using a dual-additive strategy that simultaneously programs the formation of both the anode solid-electrolyte interphase (SEI) and the cathode-electrolyte interphase (CEI). By aligning the electrolyte's highest occupied molecular orbital (HOMO) and lowest unoccupied molecular orbital (LUMO) energy levels with the cathode and anode potentials, the electrolyte undergoes spatially selective decomposition, enabling a continuous and uniform SEI/CEI pair. This programmed SEI/CEI pair expands the usable voltage window and supports deeper Mg^{2+} insertion/extraction, delivering 127.3 mAh g^{-1} (close to the theoretical capacity of Mo_6S_8, 128.8 mAh g^{-1}) in Mg||Mo_6S_8 full cells, with cycling durability competitive with state-of-the-art RMB reports. These findings establish paired-interphase programming as a general design paradigm to break the capacity-lifetime trade-off in RMBs.

View Article Online
DOI: 10.1039/D6EE01732K

Introduction

Rechargeable magnesium metal batteries (RMBs) promise a step change in safety and resource sustainability, yet progress remains limited by persistently uncontrolled interfacial evolution that is often misattributed[1–7]. Most interphase studies still adopt a single-electrode optimization paradigm, focusing either on engineering a robust anode solid-electrolyte interphase (SEI)[8–12] or on stabilizing a cathode-electrolyte interphase (CEI)[13,14]. In a practical full-cell, however, interfacial evolution is not a simple combination of two independently optimized halves. Rather, it is governed by strong electrode-electrolyte-electrode coupling (EEEC), where inadequate passivation at one electrode continuously generates mobile decomposition intermediates, reshapes electrolyte composition, and alters local charge-transfer behaviors, which in turn destabilizes the counter-electrode interphase (Figure 1a). Consequently, optimizing only one interface may not deliver the anticipated improvement. It can even be counterproductive, because parasitic reactions at the unprotected electrode can dominate electrolyte-electrode chemistry and ultimately negate, or even outweigh, the benefits gained at the engineered interface[15–18]. These considerations recast interfacial stability in RMBs from a local materials-engineering objective into a system-level coupled problem. On this basis, we highlight a critical yet underappreciated requirement: stable RMBs operation demands the simultaneous programming of paired interfaces, namely a CEI and a SEI that are co-designed to function cooperatively under EEEC (Figure 1b).

Several technical challenges remain to be addressed to realize durable battery operation. A functional interphase, particularly the SEI, must satisfy simultaneous morphological and compositional requirements[19]. Morphologically, the interphase should be continuous and laterally uniform. Non-uniform thickness concentrates ionic flux and reaction current and enables electron tunneling through thin spots, accelerating side reactions and non-uniform Mg deposition. Cracks or discontinuities expose fresh surface and promote interphase fragmentation under deep cycling, increasing polarization and rapidly eroding stability[20]. Compositionally, accumulated evidence suggests that a high fraction of fluorinated species is often beneficial for high ionic conductivity and low interfacial impedance[21,22], while an organic-inorganic composite architecture can provide the fracture resistance needed to accommodate interfacial stress and suppress cracking[23].

Rather than relying on laborious trial-and-error screening, we return to a classical yet powerful design tool, aligning the frontier orbital energies of electrolyte components with the electrochemical potentials of both electrodes to program interphase formation. Specifically, by leveraging the matching between the highest occupied molecular orbital (HOMO)/lowest unoccupied molecular orbital (LUMO) levels of electrolyte and the cathode/anode energy landscape, oxidative and reductive decomposition can be made spatially selective[24]. On the anode side, components with lower LUMO levels are preferentially reduced in a controlled manner, enabling the targeted construction of an electronically insulating yet Mg^{2+}-conducting SEI. On the cathode side, components with higher HOMO levels are preferentially oxidized to form a stable CEI. In this framework, the effective "electrochemical stability window" is no

View Article Online
DOI: 10.1039/D6EE01732K

longer dictated solely by the intrinsic thermodynamic limits of the bulk electrolyte, but is instead co-defined by the electronic structure and morphology of the interphases that emerge at each electrode[25]. Such space-programmed interphase formation can decouple interfacial electron transport from ion transport, thereby suppressing parasitic reactions and markedly improving full-cell interfacial stability.

In this work, guided by the energy-level design principle described above, we formulate a dual-additive electrolyte that enables the concurrent formation of both the SEI and the CEI. This is achieved by pairing a salt component that is preferentially reduced at the anode with one that is preferentially oxidized at the cathode. Control electrolytes containing a single salt provide a mechanistic baseline, revealing that anode-targeted formulations produce a defective SEI, whereas cathode-targeted formulations yield an uneven CEI with ion-blocking phases. In contrast, the cooperative dual-additive chemistry generates a continuous, compact, and mutually matched SEI/CEI pair, motivating a system-level electrolyte strategy for paired interphase co-regulation in RMBs.

Results

Thermodynamics of electrolytes

The narrow potential gap between Mg plating/stripping and cathode operation compresses both reductive and oxidative reactions into a confined energy range. In this landscape, we sought to disentangle how specific electrolytes govern interphase formation and stability. To this end, we focused on two model salts with contrasting oxidation/redox stabilities, $Mg(TFSI)_2$[26–28] and $Mg(PFTB)_2$[29,30]. Density functional theory (DFT) calculations of electrostatic potential (ESP) were performed on $Mg(TFSI)_2$ and $Mg(PFTB)_2$ (Figure 2a). The negative charge of $TFSI^-$ is largely delocalized across the sulfonyl framework. Multiple oxygen atoms provide multidentate coordination to Mg^{2+}, strengthening local cation-anion electrostatic interactions and inducing a more pronounced polarization of the electron density. By contrast, $PFTB^-$ shows a weaker affinity toward Mg^{2+}, leading to less stable coordination and a more labile cation-anion association. Accordingly, $TFSI^-$ is more likely to migrate together with Mg^{2+} and undergo preferential reductive decomposition at the low-potential anode, thereby contributing to SEI formation. In contrast, $PFTB^-$ exhibits a weaker affinity toward Mg^{2+}, resulting in a higher fraction of free anions in solution. It is therefore more prone to participate in oxidative decomposition and interphase-forming reactions at the high-potential cathode, promoting the growth of a CEI. The calculated energy-level alignment reveals that $TFSI^-$ possesses a deep-lying LUMO of -3.09 eV, favoring electron acceptance, whereas $PFTB^-$ exhibits an elevated HOMO of -3.31 eV, rendering it more prone to oxidative activation (Figure 2b). To rationalize the asymmetric interphase behavior of the two salts, we mapped their HOMO-LUMO energy levels onto the Mg metal Fermi level and the operating potentials of the Mo_6S_8 cathode (Figure 2c). Using a single-salt electrolyte leads to an intrinsically unbalanced interphase. $Mg(TFSI)_2$ tends to form a SEI on the anode, whereas $Mg(PFTB)_2$ preferentially decomposes at high potentials and yields a CEI on

View Article Online
DOI: 10.1039/D6EE01732K

the cathode. Crucially, the unprotected counter electrode becomes a continuous source of soluble/reactive decomposition products, which migrate across the bulk-electrolyte and undermine the interphase on the opposite electrode. As a result, apparent passivation on one side cannot be sustained unless both CEI and SEI are simultaneously stabilized. Building on these insights, we selected a magnesium aluminum chloride complex (MACC) electrolyte as the baseline system because of its well-established compatibility with Mg metal. Guided by the HOMO-LUMO energy alignment of the two additional salts, we created three electrolyte variants (Figure S1) for systematic comparison. Adding $Mg(TFSI)_2$ to the baseline produces an anode-oriented electrolyte (AOE). Incorporating $Mg(PFTB)_2$ yields a cathode-oriented electrolyte (COE). When both salts are introduced simultaneously, the resulting mixed-salt formulation does not simply broaden the intrinsic thermodynamic stability window; rather, it promotes rapid dual-interphase formation on both electrodes, which kinetically suppresses further parasitic decomposition and gives rise to a wider effective operational stability window. This mixed-salt formulation is therefore designated as the dual-electrode-oriented electrolyte (DOE).

Electrolyte-controlled interphase formation

To clarify how electrolyte chemistry governs interphase formation, transmission electron microscopy (TEM) was first employed to visualize the morphology of the CEI and SEI after 20 cycles in the three electrolytes (Figures 3a-3f). In DOE, both electrodes are uniformly passivated by continuous and conformal interphases. The Mo_6S_8 cathode is covered by a smooth and homogeneous CEI (Figure 3a), while the Mg anode develops a compact and morphologically uniform SEI (Figure 3d). In AOE, the absence of a discernible CEI leaves the Mo_6S_8 surface exposed (Figure 3b). Although an ultrathin SEI forms on Mg, its discontinuity, together with local cracking and interfacial voids, indicates insufficient electronic passivation (Figure 3e). In COE, both electrodes develop highly heterogeneous interphases. The CEI shows pronounced thickness variations with locally embedded crystalline MgO domains (Figures 3c and S2)[31,32]. The Mg surface layer is likewise nonuniform (Figure 3f). The coupled nonuniformity across both electrodes aligns with extensive interfacial side product formation and redistribution in COE.

X-ray photoelectron spectroscopy (XPS) was then used to resolve the interphase compositions on the cathode and anode (Figures S3-S6). In the cathode C 1s spectra (Figure S3a), COE shows an increased contribution from oxygenated carbon species (C-O/-C=O), indicating an organic-rich surface layer[33]. This enrichment is consistent with enhanced solvent decomposition under insufficient anode passivation, leading to the accumulation of by-products on the cathode surface. On the Mg anode, XPS spectra in the Mo 3d region show a distinct S 2s feature in AOE (Figure S3b)[34], consistent with the dissolution of cathode species and their subsequent deposition on the Mg surface in the absence of effective cathode-side protection. In addition, an extra low-binding-energy Mo 3d component assignable to Mo^{2+} is observed in both AOE and COE relative to DOE. The presence of this reduced Mo component is consistent with a more reductive anode interfacial environment arising from insufficient passivation.

View Article Online
DOI: 10.1039/D6EE01732K

To further probe the depth-resolved chemistry of the interphases on both electrodes, we combined XPS sputter profiling of the cathode CEI with Time-of-flight secondary ion mass spectrometry (TOF-SIMS) analysis of the anode SEI (Figures 4a-4g).

For the cathode, XPS sputter profiling was performed for DOE and COE to track the evolution of C 1s, O 1s, F 1s, and S 2p signals over 0 to 120 s of sputtering (Figures 4a and 4c). The DOE-derived CEI shows a stratified architecture, with an MgF_2-rich inner layer and an adsorbed organic overlayer (Figures 4b and S7a). By contrast, the COE-derived CEI is dominated by MgO and organic species throughout the probed depth (Figures 4d and S7b). Together with the morphology and surface spectroscopy results above, these observations delineate three electrolyte-dependent interphase-formation regimes, as schematically summarized in Figure S8. In DOE, the cathode interphase is stratified, comprising an inner MgF_2-rich inorganic framework that provides a continuous Mg^{2+}-conducting backbone, capped by an organic-rich outer layer that enhances mechanical compliance while limiting electron leakage (Figure S8a). In AOE, the absence of a cathode-side interphase leaves Mo_6S_8 exposed and is accompanied by substantial cathode dissolution (Figure S8b). In COE, insufficient anode-side passivation leads to pervasive electron leakage and solvent decomposition, and the resulting by-products deposit at the cathode to form an MgO- and organic-rich CEI that intrinsically constrains Mg^{2+} transport (Figure S8c). The contrast between DOE and COE further indicates that the superior CEI uniformity in DOE arises not solely from cathode-directed oxidative interphase formation, but also from the coupled stabilization of both interfaces, as improved anode passivation suppresses cross-talk and by-product deposition during CEI growth.

TOF-SIMS was further used to probe the SEI composition and its depth-dependent distribution on the Mg anodes (Figures 4e-4g and S9). In DOE, MgF^+ fragments are abundant and nearly uniform with depth, whereas MgO^- signal is weak. CH^- fragments that represent organic components are mainly concentrated at the near-surface region, indicating a layered SEI that mirrors the CEI (Figure 4e). This trend is consistent with DFT-calculated adsorption energetics of representative salt-derived fragments on Mg, where strong F^- binding favors rapid interfacial fluorination and formation of an MgF_2-rich backbone, while more weakly bound fragments preferentially reside toward the outer region (Figure S10). In COE, MgF^+ is confined to a narrow near-surface region, while MgO^- and CH^- signals remain intense throughout the SEI, indicating an MgO and organic-dominated interphase, in line with the CEI composition in COE (Figure 4g). The SEI formed in AOE exhibits intermediate characteristics, with a stronger MgF_2 signature and reduced organic contribution compared with COE (Figure 4f).

Electrochemical performance

To connect interphase chemistries with cell-level behavior, we assembled Mg||cathode cells and assessed how concurrent stabilization of both electrodes regulates the usable voltage window, interfacial kinetics, and electrochemical performance.

We first compared the voltage profiles of Mg||Mo_6S_8 cells over the first two cycles (Figure 5a). AOE displays pronounced low-voltage tails near the discharge cutoff,

View Article Online
DOI: 10.1039/D6EE01732K

while COE does not reach the upper cutoff of 2.5 V during charging (Note S1). In contrast, DOE delivers clean discharge and charge traces without obvious overdischarge or overcharge features, indicating a broader usable voltage window enabled by dual-interphase stabilization. After the electrochemical response stabilizes at the 20th cycle, DOE maintains a more sustained voltage plateau and the smallest charge-discharge hysteresis among the three electrolytes (Figure 5b), consistent with reduced polarization under dual-interphase regulation. The kinetic signatures from cyclic voltammetry (CV) reinforce this trend. Across scan rates, DOE consistently shows the strongest redox features and the smallest peak separation, whereas AOE and COE exhibit stronger peak broadening and larger peak separation as the scan rate increases (Figure 5c), consistent with progressively sluggish kinetics. Integrating the CV response to obtain the transferred charge (Q) reveals that DOE sustains the highest capacity at all scan rates (Figure 5d)[35,36].

Oxidative stability beyond the nominal operating window was next quantified by potentiostatic hold tests in Mg||Mo_6S_8 cells after 20 conditioning cycles. The cathode potential was stepped from 2.5 to 2.7 V (vs. Mg^{2+}/Mg) in 0.1 V increments (Figure 6a). DOE shows a nearly negligible and stable leakage current across the entire window, consistent with effective electronic passivation, whereas AOE and COE exhibit markedly higher leakage currents[37].

Under 1C (128.8 mA g^{-1}, based on the theoretical capacity of Mo_6S_8), Mg||Mo_6S_8 cells using DOE deliver the highest specific capacity of 127.3 mAh g^{-1} (close to the theoretical value of Mo_6S_8), and show improved capacity retention relative to AOE and COE (Figure 6b). Mg plating morphology after prolonged cycling supports this trend (Figure S11). The dQ/dV profiles at the stabilized state (20th cycle) further show the sharpest redox features and the smallest peak separation in DOE (Figure 6c), indicating reduced polarization during operation. When benchmarked against representative reports on Mg||Mo_6S_8 cells, DOE-based cells fall within the high-performance regime in both specific capacity and cycling stability[10,11,21,29,38–47] (Figures 6d, S12, and Table S1). The same electrolyte dependence extends to an organic cathode. In Mg||PANI cells, DOE provides the largest reversible capacity and a higher average discharge voltage at 1C (250 mA g^{-1}) (Figure S13), and it maintains the highest capacity with the most stable retention during cycling at 2C (Figure 6e and Figure S14).

The intrinsic stability of Mg plating and stripping in DOE is further supported by Mg||Mg symmetric cells, which sustain lower and more stable polarization and markedly longer lifetimes than AOE and COE under both moderate and high throughput cycling conditions (Figures S15 and S16). Consistently, rate tests and kinetic analysis in Mg||Mg cells yield the highest exchange current density for DOE (Figure S17), indicating accelerated interfacial charge transfer. In Mg||Mo asymmetric cells, DOE likewise shows faster Mg plating and stripping kinetics with improved reversibility relative to AOE and COE (Figures S18 and S19).

Anode stabilization in different electrolytes

The stability gap among the three electrolytes becomes most evident on the Mg surface after extended cycling, where the cumulative consequences of electrolyte

View Article Online
DOI: 10.1039/D6EE01732K

decomposition, cathode-anode cross-talk, and the resulting interphase evolution are directly reflected in the post-cycling morphology (Figures 7d-7i). The schematics in Figures 7a-7c summarize the corresponding interphase scenarios in DOE, AOE, and COE, highlighting how these coupled processes shape Mg deposition and stripping.

In DOE, the Mg surface is regulated by a spatially uniform SEI comprising an MgF_2-rich inorganic framework and an organic overlayer. This interphase supports Mg^{2+} transport while maintaining electronic passivation, thereby limiting sustained electrolyte reduction and suppressing interfacial heterogeneity during cycling (Figure 7a). The resulting uniform Mg plating and stripping preserve a smooth and dense Mg surface after cycling at both low and high magnifications (Figures 7d and 7g).

In AOE, the absence of an effective CEI on the cathode side permits progressive dissolution of Mo_6S_8 and the generation of soluble cathode-derived species during cycling. Although an SEI may initially form on Mg, these soluble species can migrate to the anode and progressively perturb its subsequent evolution through chemical exchange and surface deposition, thereby compromising interphase integrity and triggering localized attack (Figure 7b). The post-cycling Mg surface therefore becomes densely pitted, with abundant voids and corrosion-like features (Figures 7e and 7h).

In COE, insufficient passivation on the anode side leaves the initially formed interphase electronically permeable, allowing persistent electron leakage during cycling. The resulting parasitic reduction sustains electrolyte decomposition and progressively perturbs subsequent interphase evolution through ongoing growth and restructuring, thereby generating pronounced spatial heterogeneity in interphase composition and thickness (Figure 7c). The associated local variations in Mg^{2+} transport resistance and interfacial reactivity promote nonuniform Mg nucleation and subsequent plating/stripping, leading to terraced and step-like topographies after cycling (Figures 7f and 7i).

Together, these post-cycling Mg morphologies provide an integrated readout of long-term interfacial evolution. By simultaneously suppressing cathode dissolution-driven cross-talk and anode electron-leakage-driven electrolyte decomposition, DOE preserves interfacial homogeneity and sustains uniform Mg plating and stripping during prolonged cycling, whereas single-sided interphase regulation in AOE or COE leads to self-reinforcing interfacial degradation and progressively nonuniform Mg plating and stripping.

Conclusion

In summary, we demonstrate that a dual-additive electrolyte enables deterministic interphase engineering at both electrodes in RMBs. Specifically, the $Mg(TFSI)_2$-$Mg(PFTB)_2$ formulation spatially programs reductive and oxidative decomposition to form interphases that are electronically passivating while allowing Mg^{2+} diffusion. TEM reveals the formation of a continuous and laterally uniform SEI/CEI pair. XPS depth profiling combined with TOF-SIMS confirms that the SEI/CEI is stratified, featuring an inner MgF_2-rich inorganic framework, overlaid by an organic-rich outer layer. These conformal interphases suppress parasitic electrolyte reactions and electrode degradation, thereby extending the voltage window and kinetic stability. This

View Article Online
DOI: 10.1039/D6EE01732K

is evidenced by a low leakage current observed during potentiostatic hold tests of $Mg||Mo_6S_8$ cells. Consistently, cycling measurements reveal reduced polarization, while simultaneously delivering the highest specific capacity of 127.3 mAh g^{-1} at 1C (128.8 mA g^{-1}, based on the theoretical capacity of Mo_6S_8), with improved capacity retention. The interphase-enabled benefits extend beyond $Mg||Mo_6S_8$, translating directly to Mg||PANI full-cells and underscoring the generality of this strategy. More broadly, our results establish programmable interphase chemistry as a design principle for stabilizing multivalent metal batteries.

View Article Online
DOI: 10.1039/D6EE01732K

Methods

Preparation of electrolyte

All electrolyte preparations were performed in an argon-filled glovebox. Dry 1,2-dimethoxyethane (DME, Dodo chem, 5.0 mL) was used as the solvent. For the DOE electrolyte, $AlCl_3$ (2.0 mmol) was first dissolved in DME, after which $Mg(PFTB)_2$ (1.0 mmol; synthesized following the reported procedure[29]) was added. The mixture was magnetically stirred at room temperature for 30 min to give a clear solution. $MgCl_2$ (1.0 mmol) was then added, and the solution was stirred at room temperature for 12 h until it became clear and colorless. Finally, $Mg(TFSI)_2$ (1.25 mmol) was added, and the mixture was stirred for an additional 5 min to obtain the DOE electrolyte. The AOE and COE electrolytes were prepared using the same protocol, except that $Mg(TFSI)_2$ was omitted for AOE, and $Mg(PFTB)_2$ was omitted for COE. All electrolytes were used as-prepared without further purification.

Preparation of Mo_6S_8 and PANI cathode

Mo_6S_8 and polyaniline (PANI) were used as the cathode active materials. Mo_6S_8 powders were synthesized according to previous reports[48]. Commercial PANI (Alfa Aesar) was used as received. Mo_6S_8 cathodes were prepared by mixing Mo_6S_8, acetylene black and PVDF at a mass ratio of 7:2:1, whereas PANI cathodes were prepared by mixing PANI, Ketjen black and PTFE at a mass ratio of 6:3:1. For both electrodes, the active material and conductive carbon were ground with isopropanol for at least 30 min, followed by addition of the binder to obtain a processable mixture. The Mo_6S_8 mixture was cast onto carbon paper and vacuum-dried at 110 °C for 12 h before punching discs (10 mm in diameter). For PANI cathodes, the mixture was first kneaded into a dough, then roll-pressed using a fixed roll gap to form a uniform film, and finally cut into square electrodes. The active-material loading was 1.5 ± 0.5 mg cm^{-2}, and all electrodes were stored under vacuum at 60 °C until use.

Electrochemical measurement

CR2016 coin cells were assembled in an argon-filled glovebox (H_2O and O_2 < 0.01 ppm). Prior to assembly, Mg disks were polished to remove the oxide layer and subsequently wiped with ethyl alcohol until the surface was visibly clean. The prepared electrodes and polished Mg discs were used as the working and counter electrodes, respectively. Glass fiber separators (Whatman GF/D, thickness 680 μm, diameter 17 mm) were placed between the electrodes. Each cell was filled with 80 μL of electrolyte. Additionally, a Mo foil (50 μm thickness, 18 mm diameter) was placed on the outer side of the cathode to mitigate Cl^--induced corrosion of the stainless-steel cell casing on the cathode side.

The electrochemical tests of the batteries were carried out on a multi-channel battery test system (LAND CT2001A). Electrolyte polarization behavior was examined in symmetric Mg||Mg cells. Cyclic voltammetry (CV), and linear sweep voltammetry (LSV), were performed on a BioLogic VMP3 multichannel electrochemical workstation. CV and LSV were conducted in asymmetric Mg||Mo cells using Mo foil as the working electrode and Mg foil as both the counter and reference electrode, with scan rates of 20 and 10 mV s^{-1}, respectively. The exchange current density (i_0) for Mg

View Article Online
DOI: 10.1039/D6EE01732K

plating was determined using Equation (1)[49], where i denotes the current density, η is the total overpotential, F is the Faraday constant, R is the gas constant, and T is the absolute temperature.

$$i = i_0 \frac{F\,\eta}{RT2} \qquad (1)$$

Characterization

To analyze electrolyte speciation and composition, Raman spectra were collected on a LabRAM HR Evolution spectrometer (HORIBA Scientific) using a 532 nm excitation laser, FTIR spectra were acquired on a Nicolet iS50 FTIR spectrometer (Thermo Scientific) in diffuse reflectance mode, and ^{19}F NMR spectra were recorded on a Bruker 400 MHz spectrometer using DMSO-d_6 as the solvent. The solid electrolyte interphase (SEI) and cathode-electrolyte interphase (CEI) formed in cells cycled with the three electrolytes were characterized by TEM, XPS, and TOF-SIMS. For TEM and XPS analysis of both the CEI and SEI, the cathode and anode were harvested from the same Mg||Mo_6S_8 cells after 20 cycles. The morphology and structure of the interphase layers were examined by TEM on a JEM-F200 microscope operated at 200 kV. XPS measurements were performed on a K-Alpha spectrometer (Thermo Fisher Scientific) using a monochromatic Al Kα source. Ar-ion sputtering was carried out at 4 kV and 140 μA over a 3 mm × 3 mm area; the sputtering rate was calibrated on Ta_2O_5 to be 10 nm min^{-1}. Binding energies were calibrated against the C 1s peak at 284.8 eV. To probe SEI components under more stringent conditions, TOF-SIMS surface analysis and depth profiling were conducted on a NanoTOF 3 instrument (ULVAC-PHI) using Mg electrodes harvested from Mg||Mg symmetric cells after 20 cycles. X-ray diffraction (XRD) patterns were collected on a D2 Advance diffractometer (Bruker) using Cu Kα radiation to examine the structures of both cathode and anode electrodes harvested from Mg||Mo_6S_8 cells after the first cycle. The surface morphology of Mg anodes after prolonged cycling was examined by field-emission scanning electron microscopy (FESEM4000X, CIQTEK) after 200 cycles in Mg||Mo_6S_8 cells. Before characterization, all cycled cells were disassembled in an Ar-filled glovebox. The electrodes were rinsed three times with DME to remove residual electrolyte and then dried at 60 °C for 2 h in the glovebox to remove residual solvent. All measurements and sample transfers were performed under Ar to avoid exposure to air.

Computational details

Molecular electronic structures were calculated using density functional theory (DFT) as implemented in Gaussian[50]. Geometry optimizations and electronic structure calculations were performed using the B3LYP hybrid exchange-correlation functional together with the 6-31G(d) basis set[51–54]. All molecular geometries were fully optimized at this level of theory. Harmonic frequency calculations were performed at the same level to confirm that all optimized structures correspond to true local minima, with no imaginary frequencies. The energies of the frontier molecular orbitals (HOMO and LUMO) were extracted directly from the final SCF solutions and used as electronic structure descriptors.

All DFT calculations were performed using a periodic slab model with the Vienna

View Article Online
DOI: 10.1039/D6EE01732K

Ab initio Simulation Package (VASP)[55,56]. The generalized gradient approximation was used with Perdew-Burke-Ernzerhof exchange-correlation functional[57]. The projector-augmented wave method was utilized to describe the electron-ion interactions, and the plane-wave basis expansion cut-off was set to 450 eV[58]. All the adsorption geometries were optimized using a force-based conjugate gradient algorithm. Long-range dispersion interactions were included using the DFT-D3 empirical dispersion correction[59]. The Mg surface was modeled using a periodic four-layer model, with the two lower layers fixed and the two upper layers relaxed. A $p(3 \times 3)$ supercell was chosen with $3 \times 3 \times 1$ Monkhorst-Pack k-point mesh sampling for Brillouin-zone integration[60].

Data availability

All relevant data that support the findings of this study are presented in the Article and its Supplementary Information.

Acknowledgments

This work was supported by the National Key Research and Development Program of China (2023YFB3809500), the National Natural Science Foundation of China (52472246).

Author contributions

Yuhang Dai, Guanbin Gao, Qinyou An, Supervision and Conceptualization. Qinyou An, Funding acquisition. Wenwen Wang, Xinquan Ma, Writing – original draft. Wenwen Wang, Xinquan Ma, Yuhang Dai, Writing – review & editing. Chengyi Zhang, Data curation. Wenwen Wang, Weixiao Wang, Qin Su, Juncai Long, Dongyao Zhu, Jinghao Li, Ao Xu, Rui Fang, Investigation and Validation.

Conflicts of interests

The authors declare no conflict of interest.

View Article Online
DOI: 10.1039/D6EE01732K

References

1. Mohtadi, R., Tutusaus, O., Arthur, T.S., Zhao-Karger, Z., and Fichtner, M. The metamorphosis of rechargeable magnesium batteries. Joule (2021) *5*, 581–617. https://doi.org/10.1016/j.joule.2020.12.021.
2. Aurbach, D., Lu, Z., Schechter, A., Gofer, Y., Gizbar, H., Turgeman, R., Cohen, Y., Moshkovich, M., and Levi, E. Prototype systems for rechargeable magnesium batteries. Nature (2000) *407*, 724–727. https://doi.org/10.1038/35037553.
3. Li, Y., Kumar, S., Yang, G., Lu, J., Yao, Y., Kang, K., and Seh, Z.W. The contrast between monovalent and multivalent metal battery anodes. Science (2025) *389*, eadl5482. https://doi.org/10.1126/science.adl5482.
4. Hou, S., Ji, X., Gaskell, K., Wang, P., Wang, L., Xu, J., Sun, R., Borodin, O., and Wang, C. Solvation sheath reorganization enables divalent metal batteries with fast interfacial charge transfer kinetics. Science (2021) *374*, 172–178. https://doi.org/10.1126/science.abg3954.
5. Dong, H., Tutusaus, O., Liang, Y., Zhang, Y., Lebens-Higgins, Z., Yang, W., Mohtadi, R., and Yao, Y. High-power Mg batteries enabled by heterogeneous enolization redox chemistry and weakly coordinating electrolytes. Nat Energy (2020) *5*, 1043–1050. https://doi.org/10.1038/s41560-020-00734-0.
6. Li, S., Zhang, J., Zhang, S., Liu, Q., Cheng, H., Fan, L., Zhang, W., Wang, X., Wu, Q., and Lu, Y. Cation replacement method enables high-performance electrolytes for multivalent metal batteries. Nat Energy (2024). *9*, 285–297. https://doi.org/10.1038/s41560-023-01439-w.
7. Son, S.-B., Gao, T., Harvey, S.P., Steirer, K.X., Stokes, A., Norman, A., Wang, C., Cresce, A., Xu, K., and Ban, C. An artificial interphase enables reversible magnesium chemistry in carbonate electrolytes. Nature Chem (2018) *10*, 532–539. https://doi.org/10.1038/s41557-018-0019-6.
8. Chen, S., Ma, H., Du, Y., Zhang, W., and Yang, H.Y. Challenges and recent progress on anodes and their interfacial optimization towards high-performance rechargeable magnesium batteries. Materials Today (2024) *72*, 282–300. https://doi.org/10.1016/j.mattod.2023.12.002.
9. Attias, R., Salama, M., Hirsch, B., Goffer, Y., and Aurbach, D. Anode-Electrolyte Interfaces in Secondary Magnesium Batteries. Joule (2019) *3*, 27–52. https://doi.org/10.1016/j.joule.2018.10.028.
10. Li, C., Shyamsunder, A., Key, B., Yu, Z., and Nazar, L.F. Stabilizing magnesium plating by a low-cost inorganic surface membrane for high-voltage and high-power Mg batteries. Joule (2023) *7*, 2798–2813. https://doi.org/10.1016/j.joule.2023.10.012.
11. Song, X., Sun, J., Ren, W., Wang, L., Yang, B., Ning, H., Zhang, P., Caixiang, Z., Tie, Z., Zhang, X., et al. Iodine Boosted Fluoro-Organic Borate Electrolytes Enabling Fluent Ion-Conductive Solid Electrolyte Interphase for High-Performance Magnesium Metal Batteries. Angew Chem Int Ed (2025) *64*, e202417450. https://doi.org/10.1002/anie.202417450.
12. Zhao-Karger, Z., Liu, R., Dai, W., Li, Z., Diemant, T., Vinayan, B.P., Bonatto Minella, C., Yu, X., Manthiram, A., Behm, R.J., et al. Toward Highly Reversible Magnesium–Sulfur Batteries with Efficient and Practical $Mg[B(hfip)_4]_2$ Electrolyte. ACS Energy Lett. (2018) *3*, 2005–2013. https://doi.org/10.1021/acsenergylett.8b01061.
13. Wang, D., Du, X., Chen, G., Song, F., Du, J., Zhao, J., Ma, Y., Wang, J., Du, A., Cui, Z., et al. Cathode Electrolyte Interphase (CEI) Endows Mo_6S_8 with Fast Interfacial Magnesium-Ion Transfer Kinetics. Angew Chem Int Ed (2023) *62*, e202217709.

View Article Online
DOI: 10.1039/D6EE01732K

https://doi.org/10.1002/anie.202217709.

14. Shi, H., Wang, G., Wang, Z., Yang, L., Zhang, S., Dong, S., Qu, B., Du, A., Li, Z., Zhou, X., et al. Understanding the Cathode-Electrolyte Interfacial Chemistry in Rechargeable Magnesium Batteries. Advanced Science (2024) *11*, 2401536. https://doi.org/10.1002/advs.202401536.
15. Bai, M., Tang, X., Zhang, M., Wang, H., Wang, Z., Shao, A., and Ma, Y. An in-situ polymerization strategy for gel polymer electrolyte Si||Ni-rich lithium-ion batteries. Nat Commun (2024) *15*, 5375. https://doi.org/10.1038/s41467-024-49713-z.
16. Zhan, C., Wu, T., Lu, J., and Amine, K. Dissolution, migration, and deposition of transition metal ions in Li-ion batteries exemplified by Mn-based cathodes – a critical review. Energy Environ. Sci. (2018) *11*, 243–257. https://doi.org/10.1039/C7EE03122J.
17. Zhao, C., Jeong, H., Hwang, I., Li, T., Wang, Y., Bai, J., Li, L., Zhou, S., Su, C.C., Xu, W., et al. Polysulfide-incompatible additive suppresses spatial reaction heterogeneity of Li-S batteries. Joule (2024) *8*, 3397–3411. https://doi.org/10.1016/j.joule.2024.09.004.
18. Arifiadi, A., Demelash, F., Abke, N.M., Brake, T., Vahnstiege, M., Alsheimer, L., Wiemers-Meyer, S., Winter, M., and Kasnatscheew, J. Assessment of "Inverse" Cross-Talk (Anode to Cathode) in High-Voltage Li/Mn-Rich Layered Oxide || Li Cells. Adv Funct Materials (2025) *35*, 2413958. https://doi.org/10.1002/adfm.202413958.
19. Liang, Y., Dong, H., Aurbach, D., and Yao, Y. Current status and future directions of multivalent metal-ion batteries. Nat Energy (2020) *5*, 646–656. https://doi.org/10.1038/s41560-020-0655-0.
20. Chen, Y., Li, M., Jie, Y., Liu, Y., Zhang, Z., Yu, P., Li, W., Liu, Y., Li, X., Lei, Z., et al. Dynamic evolution of cathode-electrolyte interphase in lithium metal batteries with ether electrolytes. Joule (2025) *9*, 101885. https://doi.org/10.1016/j.joule.2025.101885.
21. Xiao, J., Zhang, X., Fan, H., Zhao, Y., Su, Y., Liu, H., Li, X., Su, Y., Yuan, H., Pan, T., et al. Stable Solid Electrolyte Interphase In Situ Formed on Magnesium-Metal Anode by using a Perfluorinated Alkoxide-Based All-Magnesium Salt Electrolyte. Advanced Materials (2022) *34*. https://doi.org/10.1002/adma.202203783.
22. Li, B., Masse, R., Liu, C., Hu, Y., Li, W., Zhang, G., and Cao, G. Kinetic surface control for improved magnesium-electrolyte interfaces for magnesium ion batteries. Energy Storage Materials (2019) *22*, 96–104. https://doi.org/10.1016/j.ensm.2019.06.035.
23. Lu, Y., Cao, Q., Zhang, W., Zeng, T., Ou, Y., Yan, S., Liu, H., Song, X., Zhou, H., Hou, W., et al. Breaking the molecular symmetricity of sulfonimide anions for high-performance lithium metal batteries under extreme cycling conditions. Nat Energy. (2024) https://doi.org/10.1038/s41560-024-01679-4.
24. Huang, H., Hu, Y., Hou, Y., Wang, X., Dong, Q., Zhao, Z., Ji, M., Zhang, W., Li, J., Xie, J., et al. Delocalized electrolyte design enables 600 Wh kg−1 lithium metal pouch cells. Nature (2025) *644*, 660–667. https://doi.org/10.1038/s41586-025-09382-4.
25. Goodenough, J.B., and Park, K.-S. The Li-Ion Rechargeable Battery: A Perspective. J. Am. Chem. Soc. (2013) *135*, 1167–1176. https://doi.org/10.1021/ja3091438.
26. Zhao, W., Pan, Z., Zhang, Y., Liu, Y., Dou, H., Shi, Y., Zuo, Z., Zhang, B., Chen, J., Zhao, X., et al. Tailoring Coordination in Conventional Ether-Based Electrolytes for Reversible Magnesium-Metal Anodes. Angew Chem Int Ed (2022) *61*, e202205187. https://doi.org/10.1002/anie.202205187.

27. Wang, S., Wang, K., Zhang, Y., Jie, Y., Li, X., Pan, Y., Gao, X., Nian, Q., Cao, R., Li, Q., et al. High-entropy Electrolyte Enables High Reversibility and Long Lifespan for Magnesium Metal Anodes. Angew Chem Int Ed (2023) *62*, e202304411. https://doi.org/10.1002/anie.202304411.
28. Morag, A., Chu, X., Marczewski, M., Kunigkeit, J., Neumann, C., Sabaghi, D., Żukowska, G.Z., Du, J., Li, X., Turchanin, A., et al. Unlocking Four-electron Conversion in Tellurium Cathodes for Advanced Magnesium-based Dual-ion Batteries. Angew Chem Int Ed (2024) *63*, e202401818. https://doi.org/10.1002/anie.202401818.
29. Long, J., Tan, S., Wang, J., Xiong, F., Cui, L., An, Q., and Mai, L. Revealing the Interfacial Chemistry of Fluoride Alkyl Magnesium Salts in Magnesium Metal Batteries. Angew Chem Int Ed (2023) *62*, e202301934. https://doi.org/10.1002/anie.202301934.
30. Long, J., He, Z., Zhang, G., Ding, Y., Zhang, J., Liu, P., Xu, H., Wang, R., Tan, S., An, Q., et al. Solvation Chemistry of Nonaqueous Electrolytes for Rechargeable Magnesium Batteries. Advanced Materials, (2025) e10488. https://doi.org/10.1002/adma.202510488.
31. Gu, D., Yuan, Y., Peng, X., Li, D., Wu, L., Huang, G., Wang, J., and Pan, F. Realizing high-stability anodes for rechargeable magnesium batteries *via in situ* -formed nanoporous Bi and nanosized Sn. J. Mater. Chem. A (2024) *12*, 26890–26901. https://doi.org/10.1039/D4TA04998E.
32. Li, Y., Feng, X., Yang, G., Lieu, W.Y., Fu, L., Zhang, C., Xing, Z., Ng, M.-F., Zhang, Q., Liu, W., et al. Toward waterproof magnesium metal anodes by uncovering water-induced passivation and drawing water-tolerant interphases. Nat Commun (2024) *15*, 9364. https://doi.org/10.1038/s41467-024-53796-z.
33. Xue, W., Huang, M., Li, Y., Zhu, Y.G., Gao, R., Xiao, X., Zhang, W., Li, S., Xu, G., Yu, Y., et al. Ultra-high-voltage Ni-rich layered cathodes in practical Li metal batteries enabled by a sulfonamide-based electrolyte. Nat Energy (2021) *6*, 495–505. https://doi.org/10.1038/s41560-021-00792-y.
34. Tan, J., Feng, L., Shao, J., Zhang, W., Qin, H., Liu, H., Shu, Y., Yang, L., Meng, Y., Tang, Y., et al. *In Situ* Li^+ Intercalation into Nanosized Chevrel Phase Mo_6 S_8 toward Efficient Electrochemical Nitroarene Reduction. J. Am. Chem. Soc. (2025) *147*, 10118–10128. https://doi.org/10.1021/jacs.4c14111.
35. Dai, Y., Liao, X., Yu, R., Li, J., Li, J., Tan, S., He, P., An, Q., Wei, Q., Chen, L., et al. Quicker and More Zn^{2+} Storage Predominantly from the Interface. Advanced Materials (2021) *33*, 2100359. https://doi.org/10.1002/adma.202100359.
36. Augustyn, V., Come, J., Lowe, M.A., Kim, J.W., Taberna, P.-L., Tolbert, S.H., Abruña, H.D., Simon, P., and Dunn, B. High-rate electrochemical energy storage through Li+ intercalation pseudocapacitance. Nature Mater (2013) *12*, 518–522. https://doi.org/10.1038/nmat3601.
37. Li, G.-X., Kou, R., Nguyen, A., Wang, K., Li, Y.-S., Lee, J., Kim, S.H., and Wang, D. Long-cycling lithium-metal batteries via an integrated solid–electrolyte interphase promoted by a progressive dual-passivation coating. Nat Energy (2025) *10*, 941–950. https://doi.org/10.1038/s41560-025-01803-y.
38. Keyzer, E.N., Glass, H.F.J., Liu, Z., Bayley, P.M., Dutton, S.E., Grey, C.P., and Wright, D.S. $Mg(PF_6)_2$ -Based Electrolyte Systems: Understanding Electrolyte–Electrode Interactions for the Development of Mg-Ion Batteries. J. Am. Chem. Soc. (2016) *138*, 8682–8685. https://doi.org/10.1021/jacs.6b04319.

39. Guo, Y., Zhang, F., Yang, J., Wang, F., NuLi, Y., and Hirano, S. Boron-based electrolyte solutions with wide electrochemical windows for rechargeable magnesium batteries. Energy Environ. Sci. (2012) *5*, 9100. https://doi.org/10.1039/c2ee22509c.
40. Du, A., Zhang, H., Zhang, Z., Zhao, J., Cui, Z., Zhao, Y., Dong, S., Wang, L., Zhou, X., and Cui, G. A Crosslinked Polytetrahydrofuran-Borate-Based Polymer Electrolyte Enabling Wide-Working-Temperature-Range Rechargeable Magnesium Batteries. Advanced Materials (2019) *31*, 1805930. https://doi.org/10.1002/adma.201805930.
41. Zhao, W., Pan, Z., Zhang, Y., Liu, Y., Dou, H., Shi, Y., Zuo, Z., Zhang, B., Chen, J., Zhao, X., et al. Tailoring Coordination in Conventional Ether-Based Electrolytes for Reversible Magnesium-Metal Anodes. Angew Chem Int Ed (2022) *61*, e202205187. https://doi.org/10.1002/anie.202205187.
42. He, Y., Li, Q., Yang, L., Yang, C., and Xu, D. Electrochemical-Conditioning-Free and Water-Resistant Hybrid $AlCl_3$ /$MgCl_2$ /$Mg(TFSI)_2$ Electrolytes for Rechargeable Magnesium Batteries. Angew Chem Int Ed (2019) *58*, 7615–7619. https://doi.org/10.1002/anie.201812824.
43. Tutusaus, O., Mohtadi, R., Arthur, T.S., Mizuno, F., Nelson, E.G., and Sevryugina, Y.V. An Efficient Halogen-Free Electrolyte for Use in Rechargeable Magnesium Batteries. Angew Chem Int Ed (2015) *54*, 7900–7904. https://doi.org/10.1002/anie.201412202.
44. Carter, T.J., Mohtadi, R., Arthur, T.S., Mizuno, F., Zhang, R., Shirai, S., and Kampf, J.W. Boron Clusters as Highly Stable Magnesium-Battery Electrolytes. Angew Chem Int Ed (2014) *53*, 3173–3177. https://doi.org/10.1002/anie.201310317.
45. Mohtadi, R., Matsui, M., Arthur, T.S., and Hwang, S. Magnesium Borohydride: From Hydrogen Storage to Magnesium Battery. Angew Chem Int Ed (2012) *51*, 9780–9783. https://doi.org/10.1002/anie.201204913.
46. Wang, F., Hua, H., Wu, D., Li, J., Xu, Y., Nie, X., Zhuang, Y., Zeng, J., and Zhao, J. Solvent Molecule Design Enables Excellent Charge Transfer Kinetics for a Magnesium Metal Anode. ACS Energy Lett. (2023) *8*, 780–789. https://doi.org/10.1021/acsenergylett.2c02525.
47. Ren, W., Wu, D., NuLi, Y., Zhang, D., Yang, Y., Wang, Y., Yang, J., and Wang, J. An Efficient Bulky $Mg[B(Otfe)_4]_2$ Electrolyte and Its Derivatively General Design Strategy for Rechargeable Magnesium Batteries. ACS Energy Lett. (2021) *6*, 3212–3220. https://doi.org/10.1021/acsenergylett.1c01411.
48. Lancry, E., Levi, E., Mitelman, A., Malovany, S., and Aurbach, D. Molten salt synthesis (MSS) of Cu2Mo6S8—New way for large-scale production of Chevrel phases. Journal of Solid State Chemistry (2006) *179*, 1879–1882. https://doi.org/10.1016/j.jssc.2006.02.032.
49. Guo, Y., Niu, P., Liu, Y., Ouyang, Y., Li, D., Zhai, T., Li, H., and Cui, Y. An Autotransferable g-C_3N_4 Li^+ -Modulating Layer toward Stable Lithium Anodes. Advanced Materials (2019) *31*, 1900342. https://doi.org/10.1002/adma.201900342.
50. Frisch, M., Trucks, G., Schlegel, H., and et, al (Wallingford,CT%! Gaussian 16, 2016).
51. Becke, A.D. Density-functional thermochemistry. III. The role of exact exchange. The Journal of Chemical Physics (1993) *98*, 5648–5652. https://doi.org/10.1063/1.464913.
52. Hehre, W.J., Ditchfield, R., and Pople, J.A. Self—Consistent Molecular Orbital Methods. XII. Further Extensions of Gaussian—Type Basis Sets for Use in Molecular Orbital Studies of Organic Molecules. The Journal of Chemical Physics (1972) *56*, 2257–2261. https://doi.org/10.1063/1.1677527.
53. Lee, C., Yang, W., and Parr, R.G. Development of the Colle-Salvetti correlation-energy

formula into a functional of the electron density. Phys. Rev. B (1988) *37*, 785–789. https://doi.org/10.1103/PhysRevB.37.785.

54. Hariharan, P.C., and Pople, J.A. The influence of polarization functions on molecular orbital hydrogenation energies. Theoret. Chim. Acta (1973) *28*, 213–222. https://doi.org/10.1007/BF00533485.
55. Kresse, G., and Furthmüller, J. Efficient iterative schemes for *ab initio* total-energy calculations using a plane-wave basis set. Phys. Rev. B (1996) *54*, 11169–11186. https://doi.org/10.1103/PhysRevB.54.11169.
56. Kresse, G., and Hafner, J. *Ab initio* molecular dynamics for liquid metals. Phys. Rev. B (1993) *47*, 558–561. https://doi.org/10.1103/PhysRevB.47.558.
57. Perdew, J.P., Burke, K., and Ernzerhof, M. Generalized Gradient Approximation Made Simple. Phys. Rev. Lett. (1996) *77*, 3865–3868. https://doi.org/10.1103/PhysRevLett.77.3865.
58. Kresse, G., and Joubert, D. From ultrasoft pseudopotentials to the projector augmented-wave method. Phys. Rev. B (1999) *59*, 1758–1775. https://doi.org/10.1103/PhysRevB.59.1758.
59. Grimme, S., Antony, J., Ehrlich, S., and Krieg, H. A consistent and accurate *ab initio* parametrization of density functional dispersion correction (DFT-D) for the 94 elements H-Pu. The Journal of Chemical Physics (2010) *132*, 154104. https://doi.org/10.1063/1.3382344.
60. Monkhorst, H.J., and Pack, J.D. Special points for Brillouin-zone integrations. Phys. Rev. B (1976) *13*, 5188–5192. https://doi.org/10.1103/PhysRevB.13.5188.

View Article Online
DOI: 10.1039/D6EE01732K

Figures

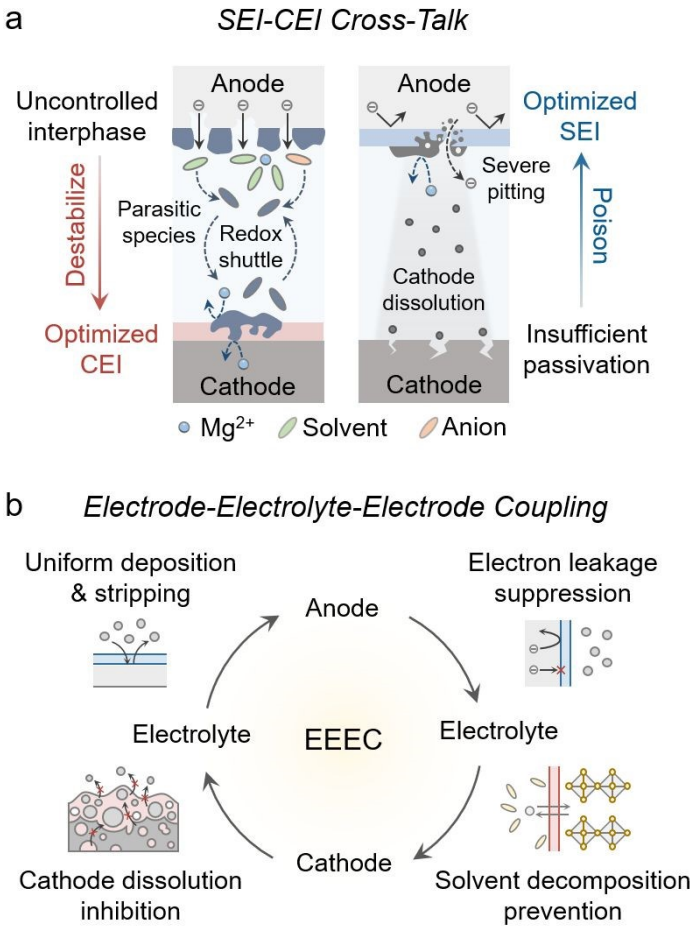

Figure 1. Schematic representation of SEI-CEI cross-talk and EEEC.
(a) Schematics illustrating that optimizing a single electrode-electrolyte interface is insufficient in full-cells. Reactive species and impurities generated at an uncontrolled interface migrate through the electrolyte and perturb the opposite, otherwise stabilized interphase, leading to interphase poisoning and accelerated parasitic reactions.
(b) Conceptual representation of electrode-electrolyte-electrode coupling (EEEC) as an intrinsic, system-level feedback loop. A stable operating regime is achieved only when the cathode, electrolyte, and anode are jointly regulated, enabling simultaneous stabilization of both CEI and SEI.

View Article Online
DOI: 10.1039/D6EE01732K

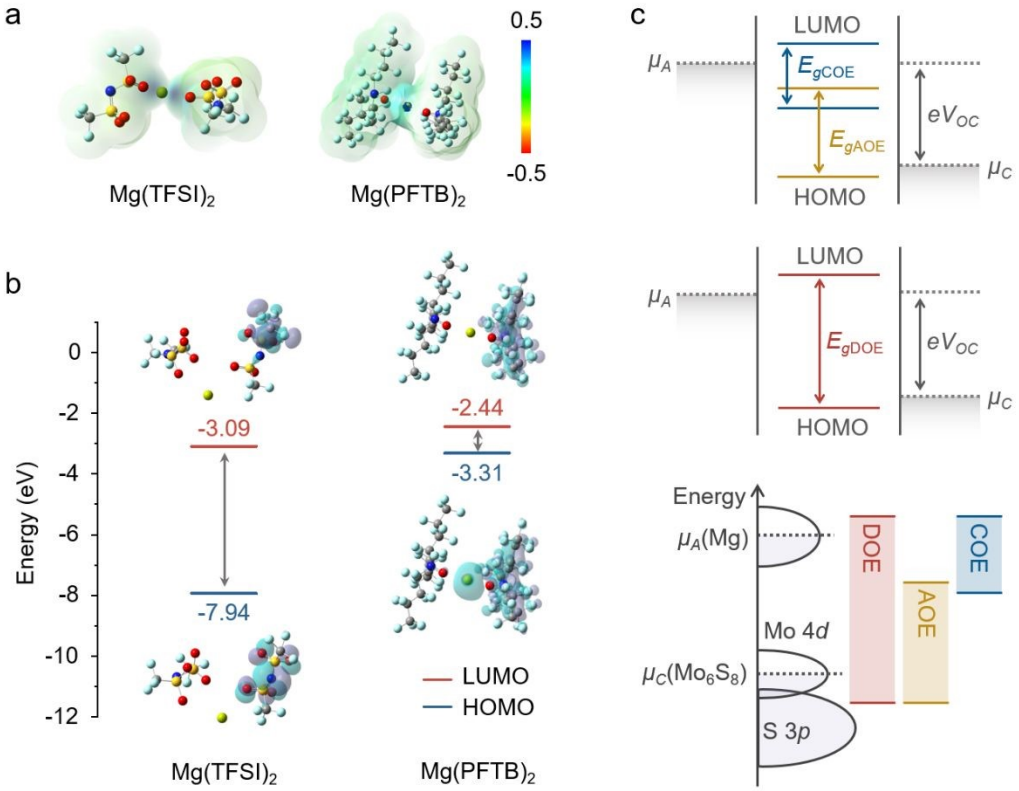

Figure 2. Energy alignment and electrolyte design

(a) ESP comparison of $Mg(TFSI)_2$ and $Mg(PFTB)_2$.

(b) The HOMO-LUMO energies of $Mg(TFSI)_2$ and $Mg(PFTB)_2$.

(c) Schematic HOMO-LUMO alignment of the three electrolytes.

View Article Online
DOI: 10.1039/D6EE01732K

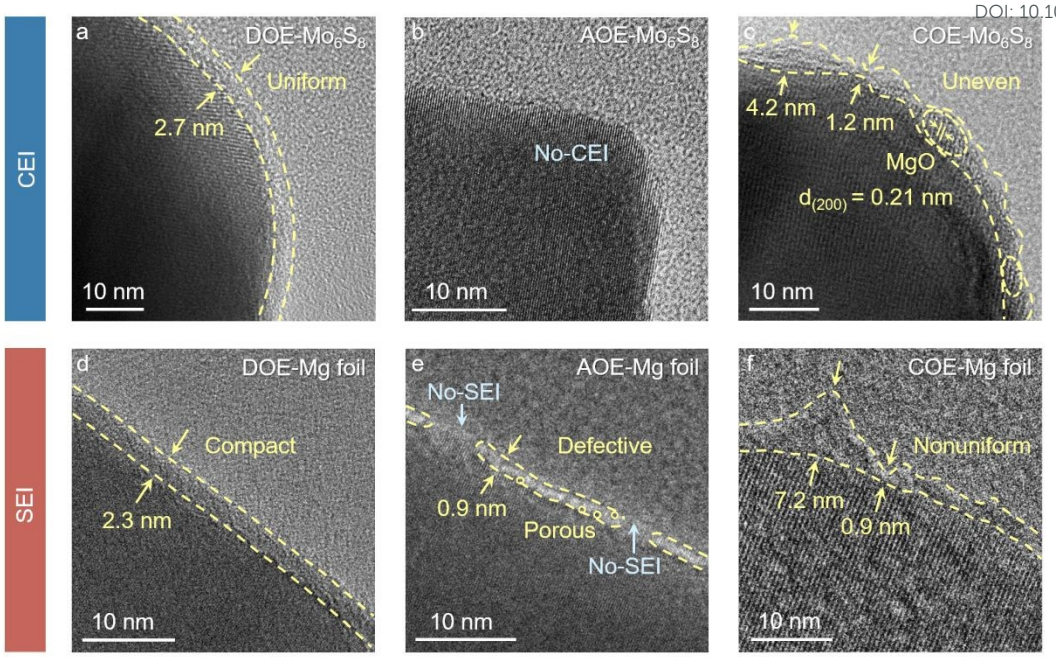

Figure 3. Interphase structural characterizations of cycled Mg||Mo_6S_8 electrodes in different electrolytes.

(a-c) TEM images of Mo_6S_8 cathodes after 20 cycles in (a)DOE, (b)AOE, and (c) COE. (d-f) TEM images of Mg anodes from the corresponding cells cycled in (d) DOE, (e) AOE, and (f) COE.

View Article Online
DOI: 10.1039/D6EE01732K

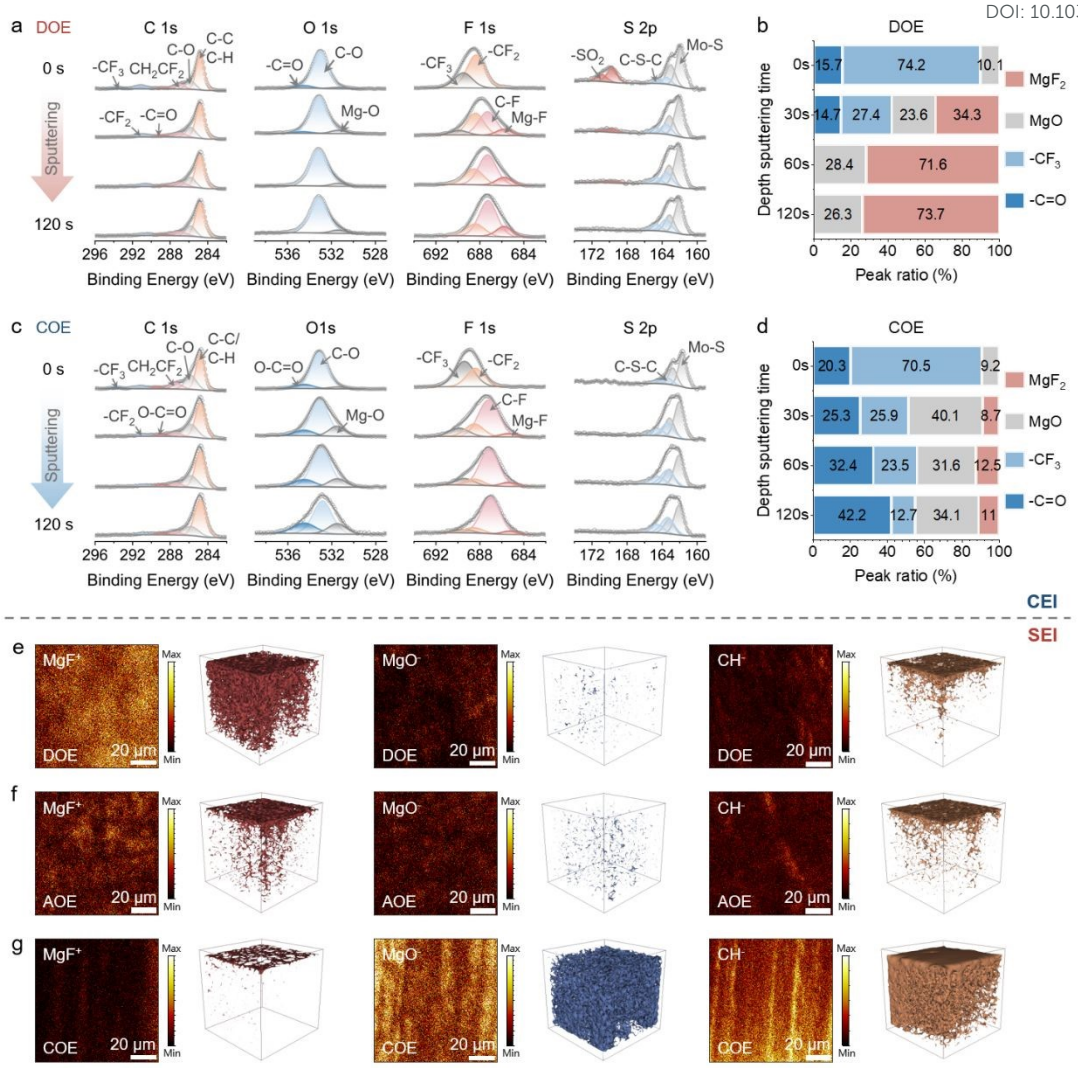

Figure 4. Compositional analysis of CEI and SEI formed in different electrolytes.
(a and c) XPS depth profiling of the CEI on Mo_6S_8 cathodes cycled in (a) DOE and (c) COE for 20 cycles.
(b and d) Depth-dependent proportions of CEI components obtained from in-depth XPS analysis for (b) DOE and (d) COE.
(e-g) TOF-SIMS 2D and 3D depth distributions of characteristic fragments in the SEI on Mg anodes cycled in (e) DOE, (f) AOE, and (g) COE after 20 cycles.

View Article Online
DOI: 10.1039/D6EE01732K

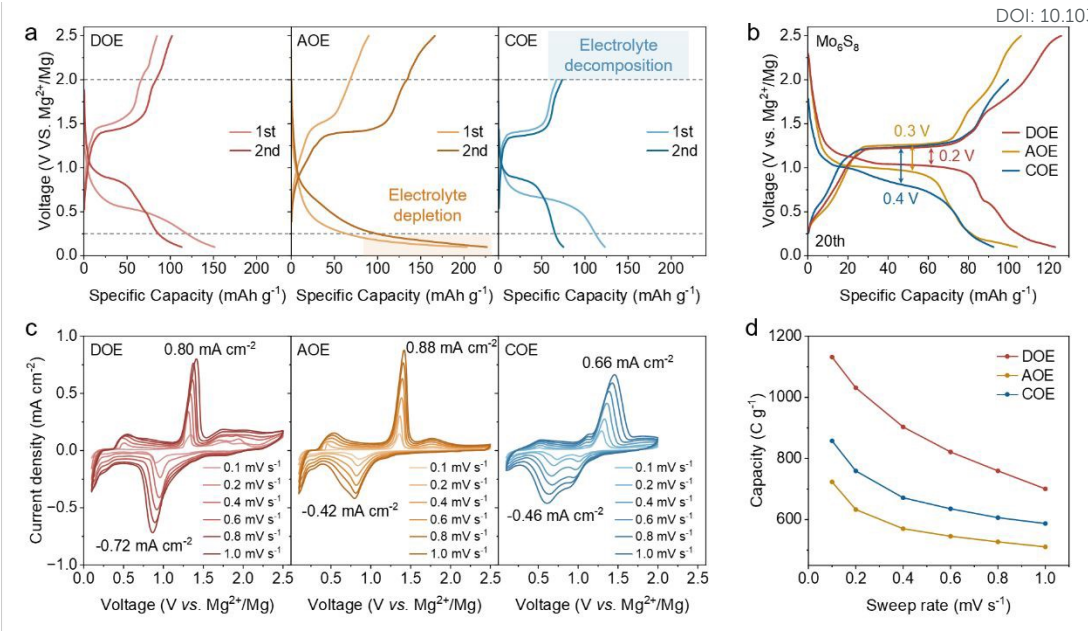

Figure 5. Electrochemical kinetic and Mg plating/stripping evaluation in different electrolytes

(a) Initial galvanostatic charge-discharge profiles of Mg||Mo_6S_8 cells in three electrolytes.

(b) Galvanostatic charge-discharge profiles at the 20th cycle after stabilization (with formed interphases) in three electrolytes.

(c) Cyclic voltammograms of Mg||Mo_6S_8 cells in the three electrolytes recorded at various scan rates.

(d) Scan-rate dependence of the specific capacity of Mg||Mo_6S_8 cells in three electrolytes.

View Article Online
DOI: 10.1039/D6EE01732K

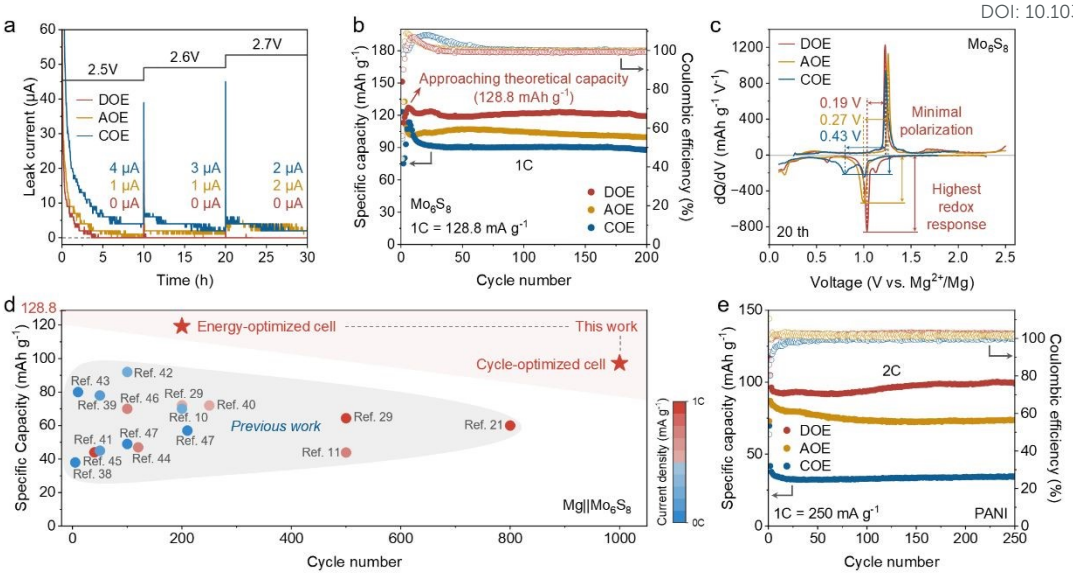

Figure 6. Interphase-regulated stability and electrochemical performance

(a) Leakage current of Mo_6S_8 cathodes during potentiostatic holds at 2.5, 2.6, and 2.7 V after 20 cycles in the indicated electrolytes, with the corresponding interphases pre-formed.

(b-c) Electrochemical behavior of Mg||Mo_6S_8 cells in three electrolytes at 1C. (b) Differential capacity (dQ/dV) profiles at the 20th cycle. (c) Cycling performance.

(d) Performance comparison of reported Mg||Mo_6S_8 cells.

(e) Cycling stability of Mg||PANI cells at 2C in three electrolytes.

View Article Online
DOI: 10.1039/D6EE01732K

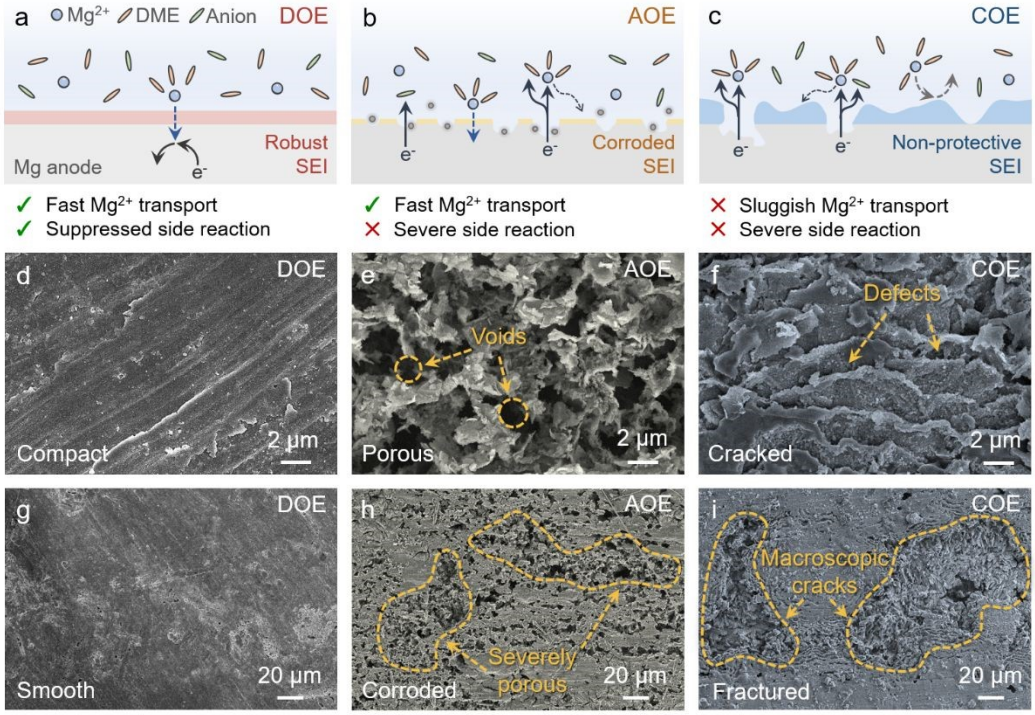

Figure 7. Magnesium deposition morphology after 200 cycles

(a-c) Schematic illustrations of Mg plating/stripping across the SEI formed in (a) DOE, (b) AOE, and (c) COE electrolytes.

(d-f) High-magnification (6000*) SEM images of Mg anodes after 200 cycles in the three electrolytes.

(g-i) Low-magnification (500*) SEM images of the corresponding Mg anodes in different electrolytes.

View Article Online
DOI: 10.1039/D6EE01732K

Data availability

All relevant data that support the findings of this study are presented in the Article and its Supplementary Information.